Int. J. Electrochem. Sci., 12 **(2017)** 11330 – 11342, doi: 10.20964/2017.12.07

International Journal of
ELECTROCHEMICAL
SCIENCE
www.electrochemsci.org

Electrodeposition of Sm-Co Alloy Films with Nanocrystalline/Amorphous Structures from a Sulphamate Aqueous Solution

Minling Xie, Liqun Zhu, Weiping Li, Huicong Liu[*]*, Tianli Zhang*[*]

Key Laboratory of Aerospace Materials and Performance (Ministry of Education), School of Materials Science and Engineering, Beihang University, No.37 Xueyuan Road, Haidian District, Beijing 100191, China
[*]E-mail: liuhc@buaa.edu.cn, tlzhang@buaa.edu.cnz

Received: 15 July 2017 / *Accepted:* 22 September 2017 / *Published:* 12 November 2017

Sm-Co alloys as permanent magnetic materials have attracted considerable interest for their application in the miniaturization of electronic devices. However, a facile method for depositing Sm-Co alloy films is still urgently needed. In this work, we exploited a simple aqueous electrodeposition approach to prepare Sm-Co films. Electrodeposition was realized by galvanostatic electrolysis from a stable sulfamate aqueous solution. The influence of the applied current density on the composition, morphology, structure and magnetic properties of the Sm-Co films was studied. Samarium was successfully incorporated into the films by the induced effect of Co(II) ions. Manipulating the current density varied the samarium content from 5.8 to 25.3 at%. Sm-Co nanosheets were discovered and were determined to have a mixed nanocrystalline/amorphous character. Furthermore, the electrodeposited Sm-Co films exhibited an obviously enhanced coercivity compared with that of other reported films.

Keywords: Sm-Co films; Electrodeposition; Aqueous solution; Nanosheets; Nanocrystalline/amorphous

1. INTRODUCTION

Sm-Co alloy, known as an important iron group rare earth permanent magnetic material, has attracted considerable attention [1, 2] owing to its excellent properties, including large saturation magnetization and coercivity [3-5], ultrahigh magnetic anisotropy [6, 7], high temperature stability [8] and moderate corrosion resistance [9]. With the growing demand for miniaturized electronic devices, thin Sm-Co films have been developed for various applications, such as high-density recording media [10, 11] and microelectronic mechanical systems [12, 13]. Several physical techniques, including sputtering [14, 15], pulsed laser [16] and plasma spray deposition, have been employed in the fabrication of Sm-Co thin films with comparatively high qualities. However, the high manufacturing cost and complex operation of these techniques limit their industrial and consumer applications. In contrast, the electrodeposition method is obviously more economical and is therefore an alternative for preparing alloy films [17-19]. In addition, the electrochemical method has several other advantages [20]. For instance, the alloy can be formed on substrates with various shapes. Moreover, the composition and phase can be appropriately controlled by modifying the electrolyte composition and deposition conditions.

Owing to the shield effect of the inner electrons on the outer electrons, the attractive force of the nucleus to the outer electrons weakens [21]. Hence, all RE (rare earth) elements, including samarium, are very active, which makes them difficult to reduce. In particular, the extremely negative equilibrium potential of samarium ($E_0<-2.3\ V_{SHE}$) is much lower than the decomposition potential of water ($2H_2O+4e \rightarrow 2OH^-+H_2$; $E_0=-0.828\ V_{SHE}$) [22]. Therefore, it is extremely difficult to electrodeposit Sm-Co alloy from aqueous solutions. Therefore, according to literature reports, substantial efforts have been devoted to exploring the use of non-aqueous solutions for electrodepositing Sm-Co alloys. Organic electrolytes [23] and molten salts [24, 25] have been exploited to electrodeposit Sm-Co alloy films. Nevertheless, the application of these two techniques is restricted by their complex equipment, environmental pollution and relatively higher cost. Thus, aqueous solution still attracts considerable interest owing to its economical and environmentally friendly advantages.

The co-electrodeposition of Sm-Co alloy from an aqueous bath has been proven possible by utilizing the induced effect of Co(II) ions with a suitable complexing agent, such as glycine [26-29]. A possible mechanism for the co-deposition Sm-Co alloys from aqueous solution was proposed by M. Schwartz [26]. That is, the dipolar (zwitterionic) features of glycine with pH fluctuation at the cathode surface may lead to the formation of hetero-dinuclear coordination complexes with complicated structures, such as $[Co^{II}Sm^{III}(Gly^-)_2(HGly^{\pm})]^{3+}$. The complexes can adsorb on the cathode surface, which facilitates the stepwise reduction of the surface-oriented Co(II) and Sm(III) cations by surface-adsorbed H atoms and/or direct electron transfer, resulting in the deposition of Sm-Co alloy. This theory is not complete and requires more evidence for verification.

To date, the electrodeposition of Sm-Co films with unique morphologies and structures from aqueous solutions has been rarely reported. A further investigation of the electrodeposition behavior is needed. Herein, we employed a sulfamate aqueous solution to electrodeposit Sm-Co alloy films, which exhibited delicate nanosheet morphologies and nanocrystalline/amorphous structures. Furthermore, the electrodeposition behavior and effect of the applied current density on the composition, surface morphology and micro-structure were thoroughly studied and discussed. Importantly, the coercivities of the as-deposited Sm-Co films were obviously enhanced compared with those of other reported films.

2. EXPERIMENTAL

All of the chemicals used in this work were of analytical grade and used without further treatment. The aqueous electrolytic bath consisted of samarium(III)-sulfamate, cobalt(II)-sulfamate

(98%, Shanghai Titan Co., Ltd, China), glycine (99.8%, Lanyi Reagent Co, China) and ammonium hydroxide. $Sm(NH_2SO_3)_3$ was prepared by the reaction of samarium oxide (99.9%, Adamas Reagent Co., Ltd) and sulfamic acid (99.5%, Aladdin Industrial Corporation). Glycine was added as a complexing agent. $NH_3{\cdot}H_2O$ was used to adjust the pH to approximately 5. Pure copper sheets (99.9%, 30 mm × 20 mm) were selected as the substrate for electrodeposition, and an insoluble platinum plate acted as the counter electrode. The plating solution contained 1 $mol{\cdot}L^{-1}$ Sm(III), 0.03 $mol{\cdot}L^{-1}$ Co(II) and 0.09 $mol{\cdot}L^{-1}$ glycine. In the following discussion, the unit of molar concentration, $mol{\cdot}L^{-1}$, is abbreviated as M. A DC current was used as the power supply for the electrodeposition process. A thermostated water bath was applied to maintain the plating bath at a constant temperature (30±1°C). Before deposition, the copper sheet surface was degreased by first dipping the sheet in acetone followed by rinsing it with flowing deionized water and ethanol. Finally, the copper substrate was dropped in sulfamic acid for several minutes to remove the oxide layer. The effective deposition time was 60 minutes. After the constant current electrodeposition process, the obtained films were washed with deionized water and ethanol and then dried in air.

All electrochemical measurements were performed using a CHI-660A electrochemical workstation. A three-electrode cell composed of a copper working electrode (area of 1 cm^2), a platinum foil counter electrode, and a Hg/Hg_2Cl_2 reference electrode (SCE) was employed. Cathodic polarization curves were recorded by the linear sweep voltammetry (LSV) technique at a scan rate of 1 $mV{\cdot}s^{-1}$. Different pairs of Sm(III)/Co(II) ion concentrations (0/0.03, 1/0.03, 1.0/0.1, and 1.0/0 M) were used to analyze the influence of the main salt on the cathodic polarization behavior. Chronopotentiometry techniques were applied to obtain E-t curves. Scanning electron microscopy (SEM, JSM-7500F, JEOL Ltd., Japan) coupled with energy dispersive X-ray spectroscopy (EDS) was used to observe the morphology and detect the chemical composition, respectively, of the obtained deposits. X-ray photoelectron spectroscopy (XPS, Thermo ESCALAB 250Xi, Al Kα radiation) was used to determine the elementary composition and check the chemical state. The phase and structure were investigated by X-ray diffractometer (XRD, D/MAX-2500). The XRD data were collected over a 2θ range from 20 to 80° at a scan speed of 6°/min with a step interval of 0.02°. Transmission electron microscopy (TEM, JEM-2100F JEOL Ltd., Japan) was used to evaluate the microstructure of the prepared films. The Sm-Co sample for TEM measurement was obtained at 40 $mA{\cdot}cm^{-2}$. The deposited film was scraped from the copper substrate and then subjected to manual grinding under the protection of ethanol. After ultrasonic dispersion, the suspension was dropped onto a carbon film to make a TEM sample. The magnetic properties were determined using a vibrating sample magnetometer (MicroMag 7407 VSM, Lake Shore, USA) at room temperature. The magnetization direction was perpendicular to the surface of the deposited film.

3. RESULTS AND DISCUSSION

3.1. Electrochemical analysis of deposition process

The characteristics of the Sm-Co electrodeposition behavior in the presence of glycine were investigated by LSV (Fig. 1(a)). Because the scanning rate of the potential was very slow (1 $mV{\cdot}s^{-1}$), the obtained curves can be approximated as steady-state cathodic polarization curves. For the Sm(III) bath (line 4), only hydrogen evolution occurred on the electrode, and no deposits were obtained, which confirmed that samarium cannot be individually electrodeposited from an aqueous solution. Nevertheless, Sm(III) could be inductively co-deposited with Co(II) [26].

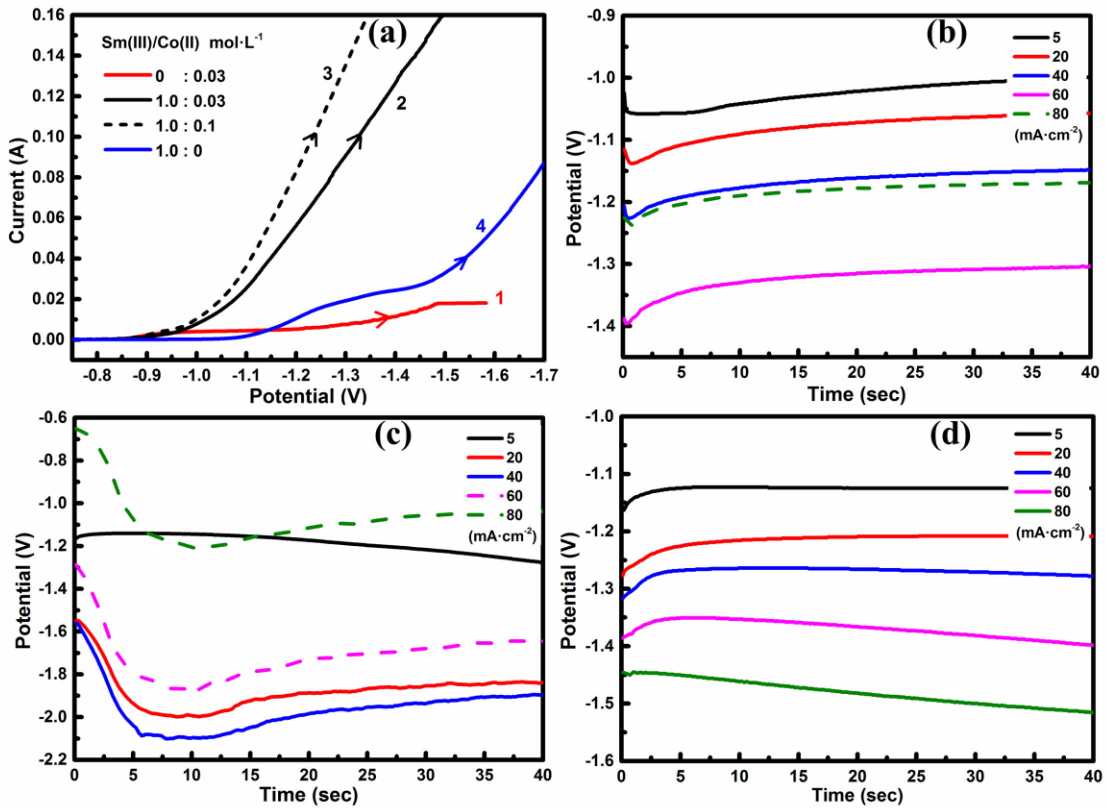

Figure 1. (a) Linear sweep voltammetry curves recorded with a Cu electrode in different baths under quiescent conditions at a scan rate of 1 mV·s^{-1}. Chronopotentiograms recorded at different current densities: (b) Sm-Co bath containing 1 M Sm(III) and 0.03 M Co(II); (c) Co bath containing 0.03 M Co(II); (d) Sm bath containing 1 M Sm(III). All solutions contained 0.09 M glycine and were kept at a pH of 5 and a temperature of 30°C.

On comparing lines 2, 3 and 4, it can be seen that when Co(II) was added to the bath, the curves significantly shifted towards more positive potentials. As expected, for a constant Sm(III) concentration, an increase in the Co(II) concentration caused a slight shift towards positive potential. This system shows the same characteristics as that of the Co-Y solutions reported by Sivaraman [30]. This shift can be ascribed to the decrease in the resistance to Co(II) reduction, which can be interpreted by the Nernst equation [31]. It was also found in our research that an increasing cobalt ion concentration in the bath gave rise to a lower samarium content in the deposits. This trend might be because when the Co(II) concentration increases, the electrode reaction is dominated by the reduction of Co(II), and hydrogen evolution decreases sharply; thus, the amount of adsorbed atomic H declines drastically, and the induced reductive effect is weakened. This interpretation matches well with the assumption put forward by Schwarz [26].

In addition, the current density value of the diffusion-controlled Co(II) reduction reaction reached an extremely low limit earlier in the Co bath owing to the low concentration of Co(II) (0.03 M). By contrast, the current limit for the Sm-Co bath rose far above that of the Co bath. These trends suggest that the addition of Sm(III) species to Co(II)-glycine solutions causes essential changes in the electrolyte solution, which ultimately affect the characteristics of the reduction process [30]. Moreover, it was observed that Sm-Co deposits began to appear on the electrode at the same potential as hydrogen evolution, so a separate reduction peak for the co-deposition of Sm-Co could not be acquired from LSV curves.

To further investigate the variation in the cathode potential during the constant current electrolysis progress, chronopotentiograms (E-t transients) were recorded at a series of current densities in the Sm-Co, Co and Sm baths, as shown in Fig. 1(b)~(d), respectively. For the bath containing only Sm(III) (Fig. 1(d)), the applied current was completely used for the hydrogen evolution reaction, and the potentials decreased to more negative values with higher current densities. Meanwhile, the E-t curves obtained in the Co bath (Fig. 1(c)) exhibited unique features when the applied current density exceeded the limiting value mentioned above. The abrupt drop in the potential when current was initially applied was due to the depletion of Co(II) ions near the electrode surface. The diffusion of Co(II) ions to the cathode surface by natural convection was no longer sufficient for maintaining the applied current density, and the potential dropped to a more negative potential until hydrogen evolution occurred [24, 31]. Subsequently, the potential slowly rose to a stable plateau. As the current density increased, the recorded curves shifted negative. However, it is interesting to observe that when the current density exceeded 40 $mA\cdot cm^{-2}$, the curves shifted in the opposite direction. This might be associated with the depolarization caused by the H^+ reduction reaction on the new cathode surface.

When Sm(III) was added to the Co(II) bath, the obtained curves exhibited a combination of the characteristics of the previous two solutions, but several important differences were also observed. First, the potential values of the curves were substantially more positive overall. Furthermore, the time to the initial potential drop was much shorter, and the extent of the drop was much smaller. It was found in the experiments that the Sm-Co co-electrodeposition reaction was accompanied by the H^+ reduction reaction even at a relatively low current density. Namely, the reduction of the hetero-dinuclear Sm(III)-Co(II)-glycine complexes and hydrogen evolution occurred at the same potential. Thus, the overpotential ($\eta=|E-Er|$, Er is the reversible potential) of hydrogen evolution in the Sm-Co bath decreased remarkably compared to that in both the Co and Sm solutions, which implies that the deposition of Sm species on the cathode (i.e., the change in the surface state of the electrode) facilitated hydrogen evolution. All of the results suggest that the inductive co-deposition of Co with Sm exhibits a unique electrochemical reduction behavior.

3.2. Morphology analysis of deposited films

Based on unaided visual inspection, the Sm-Co films obtained at a relatively low current density appeared matte gray and adhered firmly to the substrate. Meanwhile, the films obtained at a current density above 80 mA·cm^{-2} appeared dark and were poorly adhered to the substrate. The differences in color and adherence are ascribed to the composition and structure changes of the films.

Due to the incorporation of Sm into the films, obvious changes in the micro-morphology were observed (Fig. 2). The samarium-free cobalt film displayed irregular, rounded grains that appeared to be very loose and facetted (Fig. 2(a)). Sharp flake-like crystals were spread over the rounded grains. The lack of reactant near the cathode surface due to the extremely low concentration of Co(II) ions was the cause of the loose structure [30].

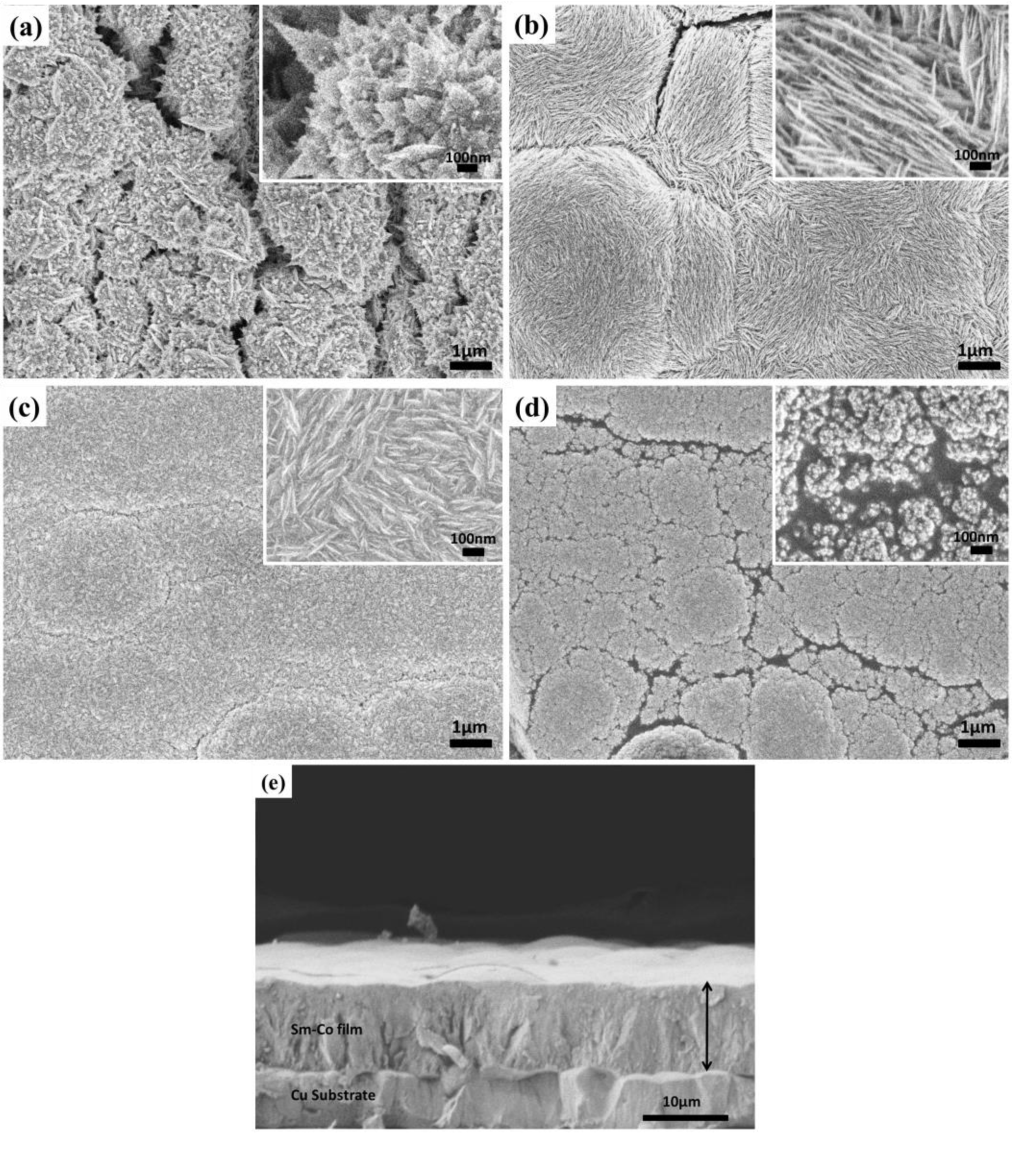

Figure 2. SEM images: (a) Co film deposited from the bath containing 0.03 M Co(II) at j=40 mA·cm^{-2}; (b, c and d) Sm-Co films deposited from the bath containing 1 M Sm(III) and 0.03 M Co(II) at j=40, 60 and 80 mA·cm^{-2}, respectively. The deposition time was 60 min. (e) Cross-sectional SEM image of a 10-μm-thick Sm-Co film obtained at j=40 mA·cm^{-2} over 100 min. The insets are the corresponding high-resolution SEM images.

However, when Sm was introduced into the film (Fig. 2(b)) by induced co-deposition, the globular grains become apparently more compact and smooth. This was also demonstrated by the compact structure observed in the cross-sectional SEM image (Fig. 2(e)). A delicate structure of tightly clustered narrow nanosheets was observed at higher magnification. Iida and Chouarbi prepared Sm-Co films with a similar micro-morphology from molten salts and an aqueous solution, respectively [20, 28]. However, the controllability and fineness of the nanostructure in our film were much better. The width of these narrow sheets was in the range of nanometers. The unique micro-morphological features may be due to the reduction of the surface-oriented Sm(III)-Co(II)-glycine complexes adsorbed on the cathode surface, which altered the electro-crystallization behavior of the Sm-Co alloy. However, the mechanism behind the significant changes in the morphology is not fully understood.

For a given bath, with an increase in the applied current density, the obtained film exhibited a finer and smoother structure (Fig. 2(c)), and the grain boundaries became more blurred. Additionally, the size of the nanosheets decreased, and they packed more tightly such that they were indiscernible, indicating the possible presence of a nanocrystalline or/and amorphous structure. This denser structure might be attributed to three factors: the greater nucleation rate at a higher overpotential, the effect of increased incorporation of samarium, and the impact of the atomic hydrogen generated from extensive water decomposition. However, when the applied current density was too high (over 80 mA·cm^{-2}, Fig. 2(d)), the film exhibited two distinct phases. The darker phase may be assigned to enriched Sm regions embedded in the metallic cobalt matrix, which is brighter. The enriched Sm regions were severely oxidized due to exposure to air.

3.3. Compositional analysis of deposited films

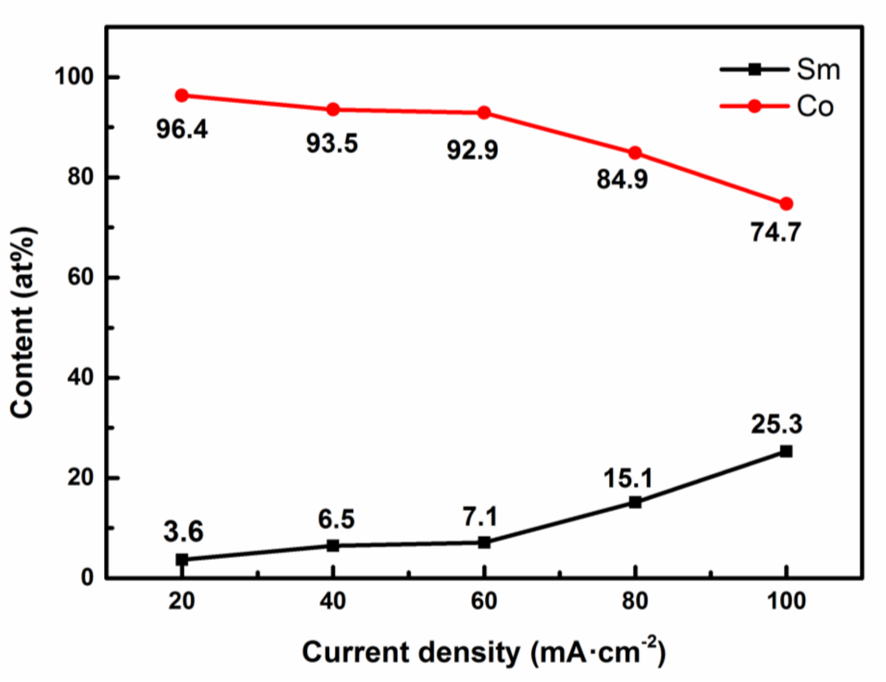

Figure 3. Influence of the cathodic current density on the content (atomic percentage) of cobalt and samarium in the deposited films. The plating bath contained 1 M Sm(III) and 0.03 M Co(II), the pH was 5, the temperature was 30°C, and the deposition time was 60 min.

As shown in Fig. 3, the composition of the Sm-Co films measured by EDS varied with the applied current density. The relative Sm/(Sm+Co) content in the deposited films increased from 3.6 at% to 25.3 at% with an increase in the current density from 20 to 100 mA·cm^{-2}. In similar reports, the effect of the current density on the composition exhibited the same trend [28, 32]. This trend might be attributed primarily to the synergistic effects of the overpotential and hydrogen evolution. A higher current density corresponds to a higher overpotential, which provides greater power for induced co-deposition. In addition, the larger amount of atomic hydrogen generated from the dominant water decomposition could promote the stepwise reduction of the hetero-dinuclear coordination complexes. It was found that the oxygen contamination of the films increased with increasing current density. Considering that samarium is too active to be easily oxidized, most of the oxygen may be derived from the oxidation of samarium on the film surface. Moreover, oxygen could also be introduced in the films in the form of hydroxide/oxide impurities due to the local increase in the hydroxide ion concentration near the cathode caused by water decomposition [22, 30].

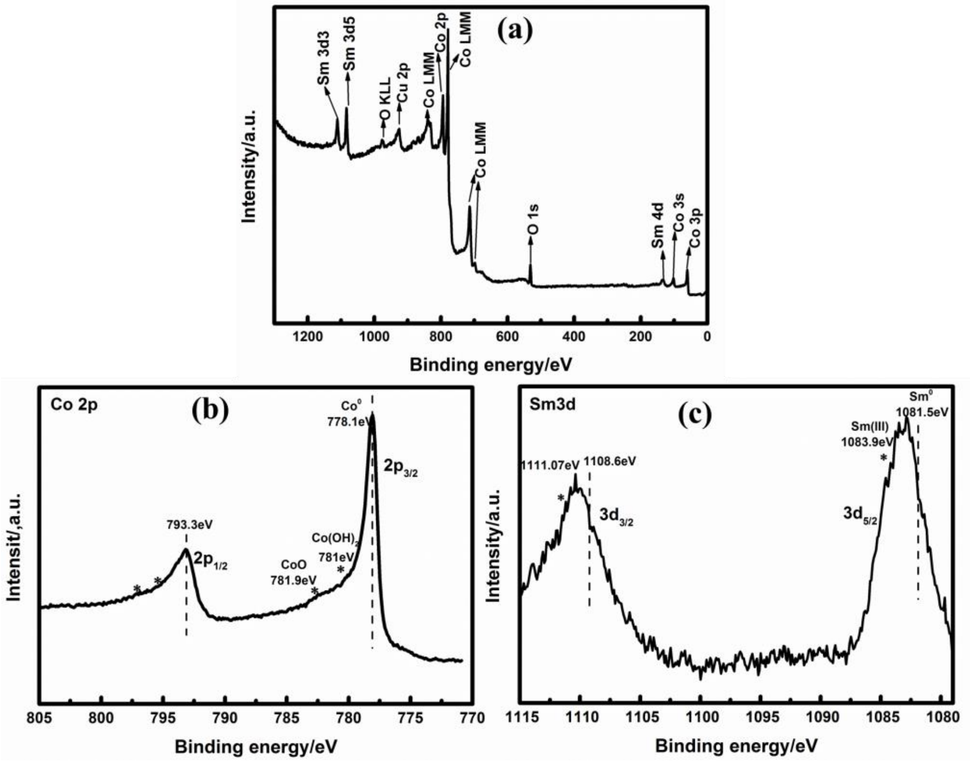

Figure 4. XPS spectra of the Sm-Co films obtained from the bath containing 1 M Sm(III) and 0.03 M Co(II) at j=40 mA·cm^{-2}: (a) survey spectrum; (b and c) high-resolution spectra of Co 2p and Sm 3d. (pH=5; T=30°C.)

To further analyze the chemical states of Sm, Co and the impurities, XPS spectra were collected, and the results are shown in Fig. 4. Fig. 4(a) shows a typical survey of the deposit, indicating the presence of Sm, Co and O, which is consistent with the EDS analyses. A copper peak belonging to the substrate was also identified. Fig. 4(b) shows the high-resolution Co 2p spectrum. Due to the multiplet splitting effect, the peak is divided into two parts, corresponding to Co $2p_{3/2}$ and Co $2p_{1/2}$.

The two obvious sharp peaks located at 778.1 eV and 793.3 eV [33] are characteristic of metallic cobalt. On the other hand, the less intense and broadened peaks denoted by asterisks are attributed to a small amount of Co^{2+} compounds. According to the literature, $Co(OH)_2$ and CoO display characteristic peaks at approximately 781 eV [34] and 781.9 eV [35], respectively. Therefore, it can be concluded that metallic cobalt was accompanied by small amounts of oxidized cobalt. In the Sm 3d spectrum (Fig. 4(c)), the binding energies for Sm $3d_{5/2}$ and Sm $3d_{3/2}$ were 1081.5 and 1108.6 eV, respectively, suggesting the presence of metallic Sm [36]. Additionally, the higher binding energies (approximately 1083.9 and 1111.07 eV) of the widened peaks may be attributed to Sm^{3+} [37], which indicates the presence of Sm-O bonds, suggesting that the surface samarium was severely oxidized.

3.4. Crystal structure

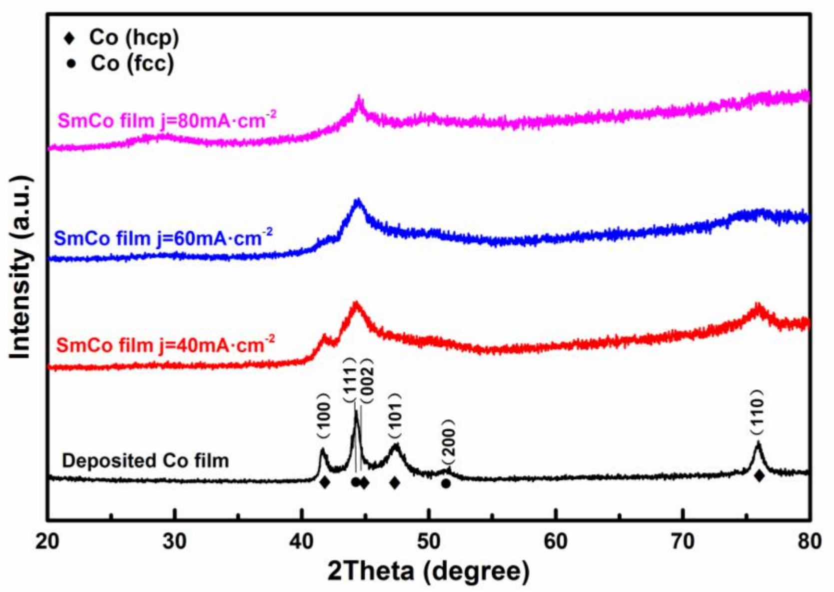

Figure 5. XRD patterns of the Co film deposited at j=40 mA·cm^{-2} from a solution containing 0.03 M Co(II) and 0.09 M glycine and of the Sm-Co films obtained at different current densities from a Sm-Co plating solution containing 1 M Sm(III) and 0.03 M Co(II). All solutions were kept at a pH of 5 and a temperature of 30°C.

The crystal structure of the deposited Sm-Co alloy films was analyzed by XRD. The patterns of the Sm-Co films deposited at different current densities as well as that of the Co film are depicted in Fig. 6. It was found that the peaks for the Co and Sm-Co deposits are rather broad and weak, indicating a nanocrystalline character and poor crystallinity of the films. In addition, the broad background in the 2θ range between 40° and 55° suggests the presence of an amorphous structure.

The main reflections of the Co film could be indexed to a hexagonal close-packed (hcp) unit cell (α-Co phase) and a face-centered cubic (fcc) unit cell (β-Co phase). For the Sm-Co films, the major peaks were derived from only the hcp α-Co phase, which is the more stable structure. With an increase in the current density from 40 to 80 mA·cm^{-2}, the Co diffraction peaks significantly broadened and even disappeared into the background, indicating grain refinement of the hcp Co phase and an increase in the amount of amorphous material in the films. The growth of amorphous Sm-Co deposits by electrochemical methods is well documented [21, 29, 38]. This type of growth might be attributed to two major factors. One is that a higher current density leads to a higher cathodic overpotential, which increases the nucleation rate during electrodeposition, eventually resulting in grain refinement and even the formation of an amorphous structure. The other factor is that a higher current density causes a relatively higher Sm content. In the process of electroreduction, Sm atoms mix into the Co lattice and hinder grain growth, leading to grain refinement or even an amorphous structure (with a high enough Sm content in the films). In addition, the extensive cathodic hydrogen evolution produces a large amount of atomic hydrogen, which can also mix into the Co lattice to promote the formation of nanocrystalline and amorphous structures.

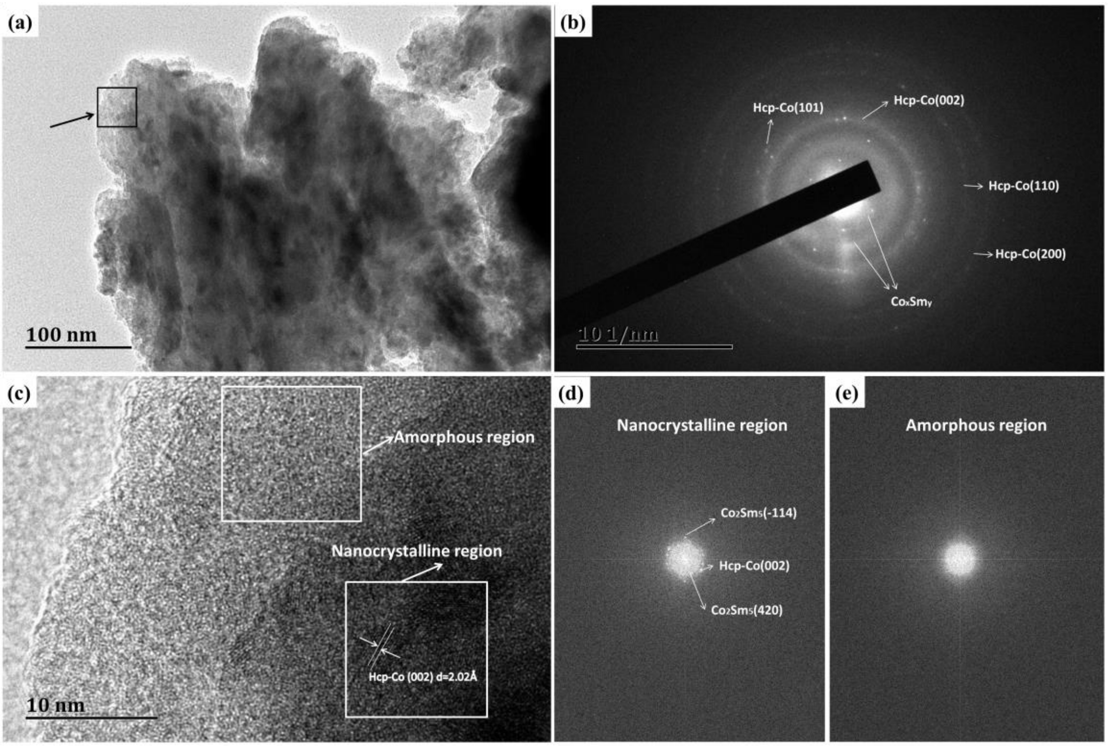

Figure 6. TEM images of a Sm-Co film deposited from the Sm-Co solution at a j of 40 mA·cm^{-2}, a pH of 5 and a temperature of 30°C: (a) bright field image; (b) SAED pattern of the region indicated by the arrow in (a); (c) HRTEM image; (d) and (e) Fast Fourier Transformation (FFT) of the amorphous and nanocrystalline regions in (c).

It is worth noting that no obvious sign of magnetic phase (Sm-Co compounds) was detected, but the EDS and XPS analyses showed the presence of a certain amount of Sm. The Sm content was more evident in the films obtained at higher current densities. This result suggests that samarium predominantly forms an amorphous phase in the films, which is detrimental to the formation of a hard magnetic phase. Hence, the deposited Sm-Co alloys could be crystallized to form alloy phases by heat treatment. This crystallization process has been confirmed in similar studies on Sm-Co and Sm–Fe alloys [13, 17].

The XRD patterns are a measure of the crystallinity of the whole Sm-Co film, whereas selected area electron diffraction (SAED) can reveal the microstructure and crystallinity of a very small area. Fig. 6 shows TEM images of the Sm-Co deposits. The SAED pattern presented in Fig. 6(b) exhibits a typical mixture of nanocrystalline and amorphous structures. The diffuse diffraction ring might be generated by an hcp α-Co phase with an extremely low crystallinity (or an amorphous Co phase). The few scattered bright diffraction spots might be derived from the few Co nanocrystallites. The inner bright rings are produced by the (002) and (101) plane of hcp α-Co, while the outer weak rings originate from the (110) and (200) plane of hcp α-Co. The innermost diffuse ring and the several spots might correspond to a small amount of Sm-Co alloy phases (Co_xSm_y, metallic compounds) produced during electrodeposition.

The high-resolution image shown in Fig. 6(c) reveals the presence of nanocrystals in the amorphous matrix. It is easy to distinguish the interatomic spacing of the nanocrystalline region. Based on calculation of the interplanar spacing, the nanocrystalline region indicated by arrow in Fig. 6(c) corresponds to hcp α-Co. This area in Fast Fourier Transformation (Fig. 6(d)) also shows a nanocrystalline character, and the main diffraction spots are derived from α-Co(002). In addition, there are several other spots that may be related to Co-Sm alloys, such as Co_2Sm_5. The amorphous region in FFT (Fig. 6(e)) shows the same amorphous character, i.e., a bright central facula without any diffraction spots. Chen also observed a mixed nanocrystalline/amorphous structure in Sm-Co nanowires electrodeposited from an ionic liquid [25]. Overall, it can be concluded from the XRD and TEM results that the deposited Sm-Co films exhibited a mixed nanocrystalline and amorphous structure. The nanocrystalline structure consisted of hcp α-Co and some Co-Sm compounds.

3.5. Magnetic properties

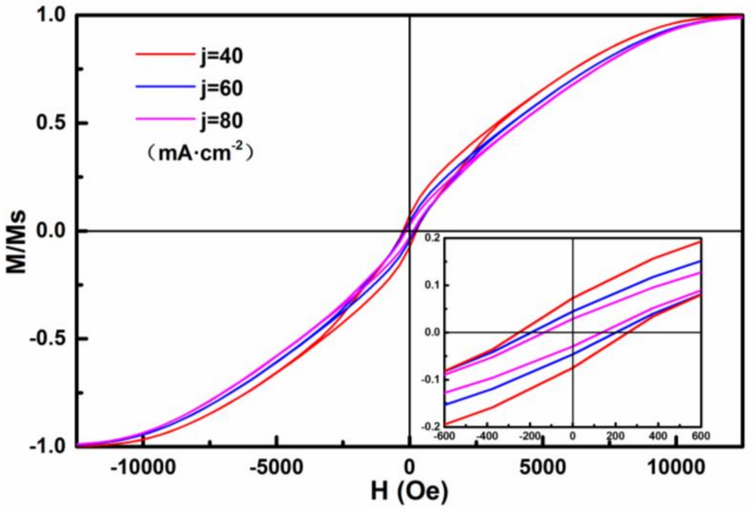

Figure 7. Room temperature hysteresis loops of the Sm-Co films electrodeposited at different current densities of 40, 60 and 80 mA·cm^{-2}. The plating bath contained 1 M Sm(III) and 0.03 M Co(II), the pH was 5, the temperature was 30°C, and the deposition time was 60 min.

The magnetic properties of the deposited Sm-Co films were measured at room temperature. Fig. 7 depicts the hysteresis loops of the electroplated Sm-Co films. With an increase in the applied current density during electrodeposition, the coercivity, *Hc*, of the Sm-Co films decreased from approximately 250 Oe to 130 Oe. The *Hc* values of these films are significantly improved over those of similar Sm-Co films (approximately 38 Oe) in which Sm_2Co_{17} was formed after heat treatment [13, 29]. The weakening of the coercivity can probably be attributed to the large amount of amorphous material in the films. The film obtained at a relatively low current density had a small amount of Sm-Co compound nanocrystallites for providing coercivity. However, the crystallinity of the Sm-Co alloy film prepared at a higher current density declined significantly, resulting in a decrease in the coercivity. In addition, the incorporation of more Sm or Co oxide impurities plays an additional role in damaging the magnetic properties. The magnetic properties of deposited RE-TM films, including Sm-Co films, are not comparable to those of Sm-Co films fabricated by physical methods [4, 21], which can be explained by the strong superparamagnetic behavior caused by the small crystal grains and amorphous structure. The oxide impurities are also likely responsible for the inferior magnetic properties.

4. CONCLUSIONS

The fabrication of Sm-Co films with a micron-scale thickness and a relatively high Sm content was accomplished by galvanostatic electrodeposition. An increase in the applied current density from 20 to 100 $mA \cdot cm^{-2}$ led to an increase in the samarium content from 3.6 to 25.3 at%. The films mainly consisted of an abundance of metallic Co and a certain amount of metallic Sm, as well as a small amount of Sm and Co oxide impurities. The Sm-Co films exhibited a promising morphology of nanosheets and a mixed nanocrystalline/amorphous structure. A higher applied current density promoted grain refinement and decreased the crystallinity. The incorporation of Sm atoms and atomic hydrogen hindered the formation of an ordered lattice, leading to a lower crystallinity. The coercivities, *Hc*, of the as-deposited films were improved over those reported for similar Sm-Co films after an annealing treatment.

ACKNOWLEDGEMENT
Funding of this research by the Key Natural Science Foundation of Beijing (Grant No. 2151002) is gratefully acknowledged.

References

1. Y. Hou, Z. Xu, S. Peng, C. Rong, J.P. Liu and S. Sun, *Adv. Mater.*, 19 (2007) 3349.
2. Y.K. Fang, H.W. Chang, Z.H. Guo, T. Liu, X.M. Li, W. Li, W.C. Chang and B.S. Han, *J. Alloy. Compd.*, 462 (2008) 376.
3. O. Gutfleisch, K.H. Müller, K. Khlopkov, M. Wolf, A. Yan, R. Schäfer, T. Gemming and L. Schultz, *Acta Mater.*, 54 (2006) 997.
4. R. Andreescu and M.J. O'Shea, *J. Appl. Phys.*, 91 (2002) 8183.
5. T.G.A. Verhagen, D.B. Boltje, J.M. van Ruitenbeek and J. Aarts, *J. Appl. Phys.*, 116 (2014) 75.

6. S. Takei, A. Morisako and M. Matsumoto, *J. Magn. Magn. Mater.*, 272-276 (2004) 1703.
7. J. Sayama, K. Mizutani, T. Asahi, J. Ariake, K. Ouchi, S. Matsunuma and T. Osaka, *J. Magn. Magn. Mater.*, 287 (2005) 239.
8. G.C. Hadjipanayis, W. Tang, Y. Zhang, S.T. Chui, J.F. Liu, C. Chen and H. Kronmuller, *Ieee. T. Magn.*, 36 (2000) 3382.
9. S. Kardelky, A. Gebert, O. Gutfleisch, A. Handstein, U. Wyss and L. Schultz, *Ieee. T. Magn.*, 40 (2004) 2931.
10. A. Morisako, I. Kato, S. Takei and X. Liu, *J. Magn. Magn. Mater.*, 303 (2006) e274.
11. A. Morisako and X. Liu, *J. Magn. Magn. Mater.*, 304 (2006) 46.
12. K. Chouarbi, M. Woytasik, E. Dufour-Gergam, E. Lefeuvre and J. Moulin, *J. Electrochem. Soc.*, 159 (2012) D529.
13. J. Chen and L. Rissing, *J. Appl. Phys.*, 109 (2011) 07A766.
14. Z. Qiu, N. Poudyal, H. Yu, G. Han, D. Zeng, J. Ping Liu and K. Zhou, *J. Alloy. Compd.*, 685 (2016) 459.
15. O. Akdogan and N.M. Dempsey, *J. Appl. Phys.*, 115 (2014) 17E508.
16. A. Singh, R. Tamm, V. Neu, S. Fähler, C.G. Oertel, W. Skrotzki, L. Schultz and B. Holzapfel, *J. Appl. Phys.*, 97 (2005) 093902.
17. C. Lou, Y. Kou, X. Lyu and W. Zhang, *Int. J. Electrochem. Sci.*, 10 (2015) 9687.
18. Y. Cao, G. Wei, H. Ge and Y. Yu, *Int. J. Electrochem. Sci.*, 9 (2014) 5272.
19. M. Zieliński, *Int. J. Electrochem. Sci.*, 8 (2013) 12192.
20. T. Iida, T. Nohira and Y. Ito, *Electrochim. Acta*, 48 (2003) 2517.
21. J. Li, H. Lai, B. Fan, B. Zhuang, L. Guan and Z. Huang, *J. Alloy. Compd.*, 477 (2009) 547.
22. J. Zhang, P. Evans and G. Zangari, *J. Magn. Magn. Mater.*, 283 (2004) 89.
23. Y. Sato, H. Ishida, K. Kobayakawa and Y. Abe, *Chem. Lett.*, 19 (1990) 1471.
24. E. Gómez, P. Cojocaru, L. Magagnin and E. Valles, *J. Electroanal. Chem.*, 658 (2011) 18.
25. Y. Chen, H. Wang and B. Li, *RSC Advances*, 5 (2015) 39620.
26. M. Schwartz, N.V. Myung and K. Nobe, *J. Electrochem. Soc.*, 151 (2004) C468.
27. J.C. Wei, M. Schwartz and K. Nobe, *ECS Transactions*, 16 (2009) 129.
28. K. Chouarbi, M. Woytasik, E. Lefeuvre and J. Moulin, *Microsyst. Technol.*, 19 (2013) 887.
29. X. Long, G. Guo, X. Li, Q. Xia and J. Zhang, *Thin Solid Films*, 548 (2013) 259.
30. K.M. Sivaraman, O. Ergeneman, S. Pané, E. Pellicer, J. Sort, K. Shou, S. Suriñach, M.D. Baró and B.J. Nelson, *Electrochim. Acta*, 56 (2011) 5142.
31. J. Schoenleber, N. Stein and C. Boulanger, *J. Electroanal. Chem.*, 724 (2014) 111.
32. K. Chouarbi, M. Woytasik, E. Dufour-Gergam, E. Lefeuvre and J. Moulin, *ECS Transactions*, 45 (2013) 15.
33. J.P. Bonnelle, J. Grimblot and A. D'huysser, *J. Electron Spectrosc.*, 7 (1975) 151.
34. I.G. Casella and M.R. Guascito, *J. Electroanal. Chem.*, 476 (1999) 54.
35. G. Giribabu, G. Murali, D. Amaranatha Reddy, C. Liu and R.P. Vijayalakshmi, *J. Alloy. Compd.*, 581 (2013) 363.
36. G. Dufour, R.C. Karnatak, J.-M. Mariot and C. Bonnelle, *Chem. Phys. Lett.*, 42 (1976) 433.
37. L. Wei, Y. Yang, X. Xia, R. Fan, T. Su, Y. Shi, J. Yu, L. Li and Y. Jiang, *RSC Adv.*, 5 (2015) 70512.
38. C. Cui, F. Chen, W. Yang, H. Li, Q. Liu and J. Sun, *Mater. Chem. Phys.*, 160 (2015) 315.